American Mineralogist, Volume 80, pages 1132–1144, 1995

Parallel electron energy-loss spectroscopy (PEELS) study of B in minerals: The electron energy-loss near-edge structure (ELNES) of the B *K* edge

LAURENCE A. J. GARVIE,* ALAN J. CRAVEN
Departments of Physics and Astronomy, University of Glasgow, Glasgow G12 8QQ, U.K.
RIK BRYDSON
Department of Materials Science and Engineering, University of Surrey, Guildford, Surrey GU2 5XH, U.K.

ABSTRACT

The B *K*-edge spectra of a wide variety of minerals have been measured using the technique of parallel electron energy-loss spectroscopy (PEELS) conducted in a scanning transmission electron microscope (STEM) from sample areas of nanometer dimensions. The B *K* edges of the minerals exhibit electron energy-loss near-edge structure (ELNES) characteristic of B coordination. For threefold-coordinated B ($^{[3]}$B), the spectra are dominated by a sharp peak at ca. 194 eV because of transitions to unoccupied states of π^* character, followed by a broader peak at ca. 203 eV attributed to states of σ^* character. The ELNES on the B *K* edge (B *K* ELNES) of fourfold-coordinated B ($^{[4]}$B) consists of a sharp rise in intensity with a maximum at ca. 199 eV followed by several weaker structures. For $^{[4]}$B, the ELNES is interpreted as transitions to states of antibonding σ^* character. Minerals that possess both $^{[3]}$B and $^{[4]}$B exhibit an edge shape that is composed of B *K* edges from the respective BO_3 and BO_4 units, and we demonstrate the feasibility of quantification of relative site occupancies in minerals containing a mixture of B coordinations. The origins of the B *K* ELNES are discussed in terms of both molecular orbital (MO) and multiple scattering (MS) theory. We also present the B *K*-edge spectra of selected nonminerals and show how differences in edge shapes and energy onsets allow these nonminerals to be readily distinguished from borates and borosilicates.

INTRODUCTION

B is impossible or difficult to analyze by the conventional techniques used by geoscientists, namely electron microprobe and X-ray fluorescence, but can be readily examined by several spectroscopic techniques. One of the most widely used bulk techniques for studying B is ^{11}B magic-angle-spinning nuclear magnetic resonance (MAS NMR), from which threefold-coordinated planar ($^{[3]}$B) triangles and fourfold-coordinated ($^{[4]}$B) sites are distinguished by their differing chemical shifts (Turner et al., 1986; Marchetti et al., 1991; Müller et al.,1993; Sills et al., 1994; Sen et al., 1994). Additional spectroscopic techniques that are used to distinguish between $^{[3]}$B and $^{[4]}$B are X-ray emission spectroscopy (XES) (Luck and Urch, 1990), Raman spectroscopy (Meera et al., 1990), and infrared spectroscopy (Moustafa et al., 1994). A few electron energy-loss spectroscopy (EELS) and X-ray absorption spectroscopy (XAS) studies have been performed on B-bearing minerals (Brydson et al., 1988b, 1988c; Sauer et al., 1993) but have mainly concentrated on inorganic materials such as BF_3 and KBF_4 (Hallmeier et al., 1981; Schwarz et al., 1983). XES and EELS studies on the unoccupied states of B were reviewed by Garvie (1995). These early studies illustrated the large differences in the B *K*-edge shapes from $^{[3]}$B and $^{[4]}$B.

Spectroscopic techniques, such as XES and X-ray photoemission spectroscopy (XPS), have become established methods for probing the occupied electronic states (mainly bonding states) of minerals. To develop a more complete understanding of the properties of minerals, such as their electronic, thermal, and optical behavior, it is necessary to investigate the unoccupied, mainly antibonding states. Until recently, the study of occupied states in minerals has commanded most attention. Unoccupied states may be probed by a variety of spectroscopic techniques, including XAS, EELS, bremsstrahlung isochromat spectroscopy (BIS), inverse photoelectron spectroscopy (IPES), and X-ray Raman spectroscopy (Fuggle and Inglesfield, 1992). Of these spectroscopic techniques, EELS and XAS are most suited to mineral studies.

Recent improvements in EELS instrumentation have resulted in renewed interest in the study of the electron energy-loss near-edge structure (ELNES) of core-loss edges from solid-state materials. EELS performed in a conventional or scanning transmission electron microscope (CTEM or STEM) is a valuable technique for determining solid-state information, such as elemental compositions, coordinations, valences, and spin states of atoms.

* Present address: Department of Geology, Arizona State University, Tempe, Arizona 85287-1404, U.S.A.

0003–004X/95/1112–1132$02.00

One of the benefits of EELS as an analytical technique is its ability to probe materials at high-spatial resolution, which facilitates the study of multiphase systems and even allows one to probe bonding at interfaces (Bruley et al., 1994) or directly identify single atomic columns (Browning et al., 1993). Parallel detector systems have recently become available for EELS (PEELS), and this has greatly increased the ease of ELNES collection and vastly extended the range of materials that may be studied. Under the correct experimental conditions, the ELNES is the result of dipole-allowed transitions from atomic core-level states to unoccupied states above the Fermi level. The ELNES often exhibits a shape that is characteristic of the arrangement and types of atoms surrounding the excited atom. This "fingerprint" of the local coordination arises in cases where there is a localized electronic interaction of the central excited atom with the atoms in the nearest-neighbor coordination sphere. The experimental basis for the ELNES coordination fingerprint is that the basic edge shape for a particular atom in a specific coordination should be similar regardless of the material in which the atom is bonded.

Several EELS and XAS studies have demonstrated the coordination fingerprint technique: Si $L_{2,3}$ edge in the SiO_4 unit (McComb et al., 1991; Li et al., 1993; Garvie et al., 1994); the C *K* edge in CO_3^{2-} (Garvie et al., 1994, 1995); the P, S, and Cl $L_{2,3}$ edges in PO_4^{3-}, SO_4^{2-}, ClO_4^-, respectively (Sekiyama et al., 1984; Hofer and Golob, 1987; Brydson et al., 1992); the Al $L_{2,3}$ and *K* edges of $^{[4]}$Al and $^{[6]}$Al (Hansen et al., 1992; Ildefonse et al., 1992, 1994); and the B *K* edge of $^{[3]}$B and $^{[4]}$B (Sauer et al., 1993). The concept of the coordination fingerprint must be used with care because the exact symmetry of the ions surrounding the excited atom can have a large effect on the shape of the ELNES, as has been demonstrated for the Si $L_{2,3}$ edge in both zircon (McComb et al., 1992) and forsterite (McComb et al., 1991). In zircon and forsterite the large angular variance of the SiO_4 tetrahedra causes the Si $L_{2,3}$ ELNES to exhibit edge shapes different from those in minerals such as α-quartz or talc, in which the angular variance of the SiO_4 tetrahedron is small.

B is present in many minerals, bonded almost exclusively to O or OH anions and only rarely to other anions such as F. In minerals, B is present in the two anions, the tetrahedral BO_4^{5-} and the planar triangular BO_3^{3-} groups. The O may be partially or totally replaced by OH anions. B triangles and tetrahedra join in a multitude of ways to form many polynuclear anions, and these polyanions in turn can polymerize to form infinite sheets, chains, and three-dimensional networks (Christ and Clark, 1977; Farmer, 1982; Heller, 1986). In the borosilicates, B substitutes for Si. This is exemplified by datolite, in which SiO_4 tetrahedra are replaced by $BO_3(OH)$ tetrahedra.

In this study, we investigate the B *K* edges of minerals containing planar $^{[3]}$B and $^{[4]}$B. We demonstrate that the coordination of the B in the minerals is unequivocally identified from the ELNES observed at the B *K* edges. Where mixed B-O coordinations are present in the same mineral, we demonstrate that the $^{[3]}$B/$^{[4]}$B ratio can be determined from the B *K* ELNES. In several of the materials the B *K* edge exhibits structure related to the distortion of the B-O polyhedron.

Materials and experimental details

Minerals containing either $^{[3]}$B or $^{[4]}$B were studied (Table 1), as were minerals with both $^{[3]}$B and $^{[4]}$B. For comparison, crystalline B and several B-containing materials (Table 1) were studied to illustrate some of the other possible B *K*-edge shapes. The minerals used in this study come from a variety of sources and have been identified by powder X-ray diffraction. All minerals, except for dumortierite and sussexite, were single crystals. Of the nonminerals, cubic BN (c-BN) was studied as single crystals, whereas the other compounds were either chips (crystalline B) or high-purity powders.

Samples for PEELS analysis were prepared by crushing selected grains in acetone. A drop of the finely divided material, suspended in acetone, was then dried on a lacy carbon film supported on a Cu TEM grid. Data were then acquired from thin areas overhanging the holes in the lacy carbon film.

PEELS spectra were recorded on a VG HB5 STEM. This microscope is equipped with a cold field-emission gun (FEG) and postspecimen lenses and operated at an accelerating voltage of 100 kV with a probe semiangle of 11 mrad and a collection angle of 12.5 mrad. The exact acquisition parameters for the spectra depended on the stability of the sample under the electron beam. In general, data were recorded from areas ranging from 130 × 100 nm^2 to 32 × 25 nm^2, using a probe current of ca. 0.5 nA with recording times of ca. 2–4 s.

Great care must be taken when recording the B *K*-edge spectra of $^{[4]}$B-containing minerals, especially those that are hydrated, because these minerals are susceptible to electron-beam damage. This damage is a result of the ease with which $^{[4]}$B converts to $^{[3]}$B by electron-beam irradiation. Sauer et al. (1993) studied the radiation damage of the mixed BO_3^-- and BO_4^--containing minerals colemanite and howlite. The initial B *K* ELNES of these minerals were consistent with their expected $^{[3]}$B/$^{[4]}$B ratio. Prolonged electron-beam irradiation of these borates produced B *K* ELNES consistent with $^{[3]}$B only.

The susceptibility to electron-beam damage of $^{[4]}$B-containing minerals studied in this work varied enormously. Anhydrous minerals such as sinhalite and rhodizite were beam stable even after prolonged irradiation. Preobrazhenskite, and especially tunellite, rapidly suffered electron-beam–induced effects accompanied by the growth of the $^{[3]}$B π^* peak. To reduce the effects of beam damage, the data were recorded with a defocused probe. The beam-sensitive minerals, such as tunellite, required special procedures for the acquisition of PEELS spectra. These procedures involved the use of short integration times (<2 s), a defocused probe, and continuous movement of the scanned area over the sample during acquisition. The majority of the B-containing nonminerals, with the ex-

TABLE 1. Experimental materials

Mineral name	Structural formula	Reference*
	[3]B-bearing minerals	
Dumortierite	$(Al,Fe)_7O_3[(BO_3)(SiO_4)_3]$	Moore and Araki, 1978
Hambergite	$Be_2(OH)(BO_3)$	Zachariasen et al., 1963
Ludwigite	$(Mg,Fe^{2+})_2Fe^{3+}O_2(BO_3)$	Bonazzi and Menchetti, 1989
Sussexite	$Mn_2(OH)[B_2O_3(OH)]$	Hoffmann and Armbruster, 1995
Gaudefroyite	$Ca_4Mn_3O_3(CO_3)(BO_3)_3$	Garvie et al., in preparation
	[4]B-bearing minerals	
Datolite	$Ca_4[B_4(SiO_4)_4(OH)_4]$	Foit et al., 1973
Danburite	$Ca[BSiO_4]_2$	Phillips et al., 1974
Axinite	$(Ca,Mn,Fe^{2+})_3Al_2[Si_2O_6][Si_2O_6BO_3(OH)]$	Takeuchi et al., 1974
Sinhalite	$MgAl(BO_4)$	Hayward et al., 1994
Rhodizite	$(Cs,K)Be_4Al_4B_{11}O_{26}(OH)_2$	Pring et al., 1986
	[3]B- and [4]B-bearing minerals	
Chambersite	$Mn_3Cl[B_7O_{13}]$	Honea and Beck, 1962
Boracite	$Mg_3Cl[B_7O_{13}]$	Dowty and Clark, 1973
Tunellite	$Sr[B_6O_9(OH)_2]\cdot 3H_2O$	Clark, 1964
Preobrazhenskite	$Mg_3[B_{11}O_{14}(OH)_8]\cdot H_2O$	Burns and Hawthorne, 1994
	B-containing nonminerals	
β-rhombohedral B	β-B_{105}	Hoard et al., 1970
Chromium boride	CrB_2	Guy and Uraz, 1976
Glassy boric oxide	B_2O_3	Prabakar et al., 1990
Hexagonal boron nitride	h-BN	Pease, 1950
Cubic boron nitride	c-BN	Solozhenko et al., 1990

* Structural reference where appropriate. No structure refinement was conducted for chambersite.

ception of glassy B_2O_3, which was beam sensitive, were sufficiently beam stable to allow the use of integration times of up to 10 s.

The following data-processing steps were performed on the spectra, as recorded: the dark current was subtracted; a background of the form AE^{-r} was subtracted from beneath the core-loss edges; and the effect of the tailing of the zero-loss peak was deconvoluted from the core-loss edge using the Fourier-ratio technique. The effects of multiple inelastic scattering were not deconvoluted from the core-loss edges because such scattering typically affects the structures approximately 20 eV above the edge onset, i.e., above the region presented for qualitative comparison of ELNES. For a more detailed discussion of EELS data processing, see Egerton (1986).

RESULTS

Minerals

The B *K* edges of the minerals that contain single-coordinated B are illustrated in Figures 1 and 2, which show minerals containing [3]B and [4]B, respectively. Large differences between the ELNES of the two B coordinations are apparent. Minerals with [3]B have ELNES dominated by an intense sharp peak at ca. 194 eV (peak A), called the π^* peak, followed by a broader peak with a maximum at ca. 203 eV (peak C), called the σ^* peak. The reasons for the use of these names will be given in the next section. Minerals that contain only [4]B have an ELNES dominated by an initial sharp rise in intensity with a maximum at ca. 199 eV (peak A). Table 2 gives the energies of the principal features for selected minerals.

None of the minerals in Figure 1 has been studied previously by PEELS, although our spectra are similar in shape to the spectra from other materials with [3]B (Ishiguro et al., 1982; Schwarz et al., 1983; Hallmeier et al., 1981; Esposto et al., 1991; Sauer et al., 1993). There are no major differences between the shapes of the π^* peak from the minerals in Figure 1, although the width at half height of this peak varies from 0.6 eV (dumortierite) to 1.5 eV (gaudefroyite). The structure of the σ^* region varies considerably among the minerals studied. Dumortierite and sussexite exhibit a broad structureless peak with a maximum centered at ca. 204 eV. For dumortierite, the lack of structure in this region may be a result of the poor counting statistics caused by its low B content, which is typically in the range 1–6 wt% B_2O_3. The σ^* regions of ludwigite, hambergite, and gaudefroyite exhibit maxima at several energy losses (Table 2). The shape of the σ^* region of hambergite is different from that of previously described [3]B-containing minerals because the intensity rises greatly to a sharp peak at 200.6 eV before gradually dropping. The height of the π^* peak is significantly more intense than the σ^* peak in dumortierite, ludwigite, sussexite, and hambergite. The ratio of the peak heights π^*/σ^* varies with 1.2 in gaudefroyite, 2.8 in dumortierite, 3.4 in sussexite, 4.1 in hambergite, and 4.9 in ludwigite. Although the intensity of the π^* peak relative to the σ^* region is often sensitive to crystal-orientation effects, especially in the case of hexagonal BN (h-BN), such effects alone cannot account for the large differences exhibited between the spectra of hambergite and gaudefroyite.

Of the spectra illustrated in Figure 2, only rhodizite has been previously studied by PEELS (Brydson et al., 1988c). Our B *K*-edge spectrum from rhodizite exhibits the same structure as the spectrum from the earlier PEELS study.

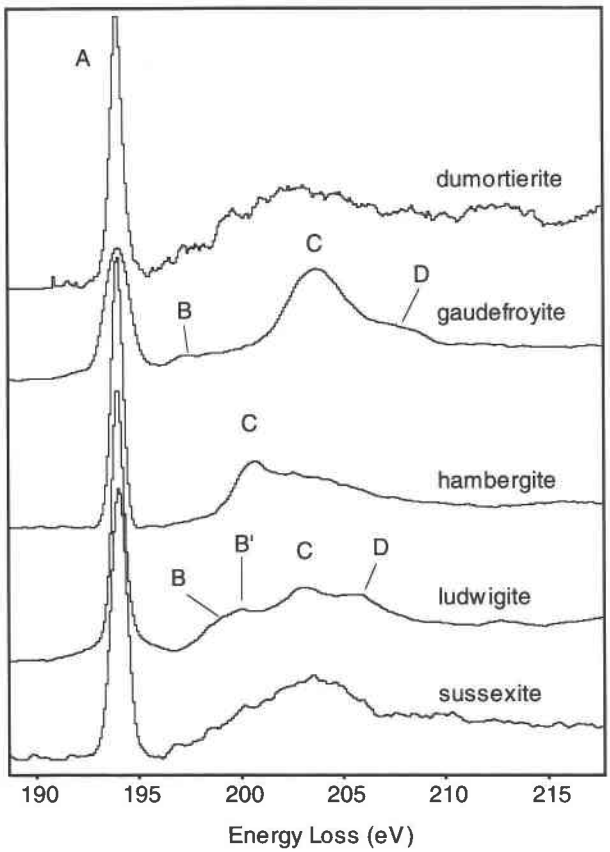

Fig. 1. Experimental PEELS B *K*-edge spectra for [3]B-containing minerals. The spectra presented here and in the following figures are shown on an arbitrary intensity scale. The labels in this figure and subsequent figures refer to major or important features described in the text.

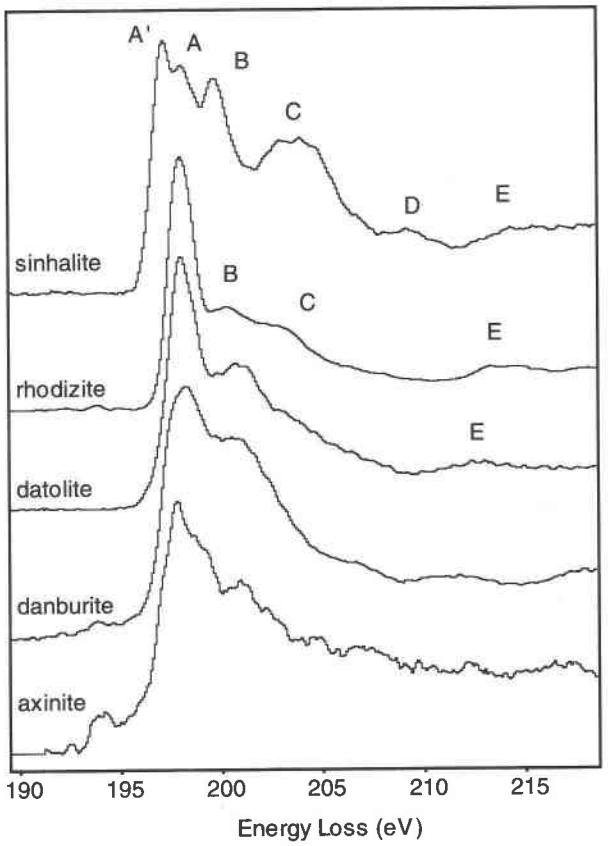

Fig. 2. Experimental PEELS B *K*-edge spectra for [4]B-containing minerals. The small prepeak observed at ca. 194 eV in rhodizite, danburite, and axinite is due to electron-beam damage.

All the minerals exhibit peaks A and B. After peak B the spectra differ in the number of peaks visible, but, except for the sinhalite spectrum, these additional peaks are broad and weak. Rhodizite, danburite, and axinite exhibit a weak peak at ca. 194 eV, which, as we saw above, is indicative of [3]B. This weak peak is caused by electron-beam damage during data acquisition. Sinhalite differs from the rest of the spectra illustrated in Figure 2 by exhibiting an additional distinct peak, A′, below peak A. As we shall see later, the intensity of peak A′ varies greatly depending on the orientation of the electron beam with respect to the principal axes of the crystal. The poor quality of the spectrum from axinite is a result of the low B content of this mineral.

Nonminerals

The B *K*-edge spectra of a variety of nonminerals are shown in Figure 3, and the energies of the major features are tabulated in Table 2. Elemental B occurs as several allotropes, the most stable of which is the β-rhombohedral form (β-B_{105}) containing 105 atoms in the unit cell (Hoard et al., 1970). The B *K* edge of β-B_{105} is similar in shape to published data (Esposto et al., 1991) and to the *K* edges of elemental Li and Be (Garvie, unpublished data). The initial sharp peak at 190.0 eV is followed by a broader maximum at ca. 196 eV. The initial sharp peak is broadened on the low-energy side and can be modeled as

Table 2. Energies (eV) of the principal features of selected materials illustrated in Figures 1–3

[3]B-containing materials	Peaks							
	A	B	B′	C	C′	D	D′	E
Gaudefroyite	193.7	197.0	—	203.4	—	207	—	—
Hambergite	194.4	—	—	201.1	—	—	—	—
Ludwigite	194.0	198.4	200.0	203.1	—	205.6	—	—
Glassy-B_2O_3	194.1	197.5	—	202.7	—	—	—	—
h-BN	192.1	194.7	—	198.3	199.5	204.4	207	215.3

[4]B-containing materials	Peaks					
	A′	A	B	C	D	E
Sinhalite	197.1	197.9	199.5	203	209	214
Rhodizite	—	198.0	200.3	203	—	213.3
Datolite	—	197.7	200.5	—	—	212
Danburite	—	198.1	200	—	—	—
c-BN	194.2	197.0	199.8	203.9	209.2	214.0

Note: Error in EELS values is ±0.2 eV.

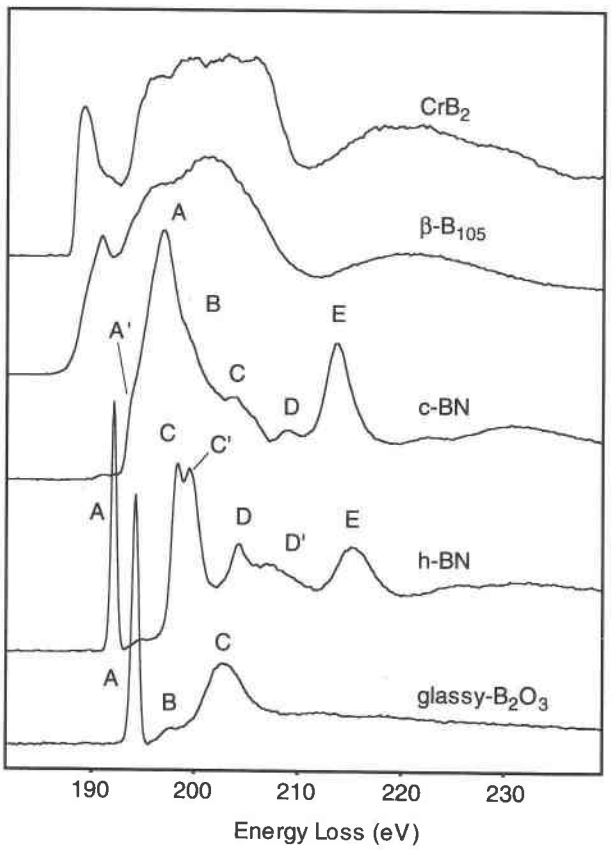

Fig. 3. Experimental PEELS B *K*-edge spectra for nonminerals; β-B_{105} = β-rhombohedral B, c-BN = cubic-BN, and h-BN = hexagonal-BN.

two peaks separated by 1.44 eV. These two peaks are probably the result of core-hole effects. As expected, the B *K*-edge onset in β-B_{105} is lower in energy than that found in [3]B- and [4]B-containing materials, in which B possesses an effective positive charge.

Chromium diboride has a B *K* ELNES similar in shape to B, although the first peak in CrB_2 is more pronounced and at a lower energy, 188.6 eV. The lower energy of the first peak in the diboride, relative to that in elemental B, may be rationalized by consideration of the charge transfer from the Cr to the B. The initial peak at 188.6 eV in the diboride represents transitions to a π^* antibonding state resulting from the presence of sp^2 bonding within the structure, whereas the following structure, centered at ca. 200 eV, may be associated with transitions to σ^* antibonding orbitals. In the diboride, B is present in layers of [3]B, each B atom being sp^2 bonded to three other B atoms. The B planes are sandwiched between layers of Cr atoms.

Boron nitride occurs in two principal polymorphs: hexagonal (h-BN) and cubic (c-BN). Hexagonal BN is a layered material with B atoms bonded to three N atoms within the plane. Cubic BN has a diamond-like structure with each B atom bonded to four N atoms. Hexagonal BN (containing [3]B) and cubic BN (containing [4]B) exhibit B *K*-edge spectra that are qualitatively similar to those from the minerals. This resemblance is rationalized by the similar electronegativities of the N and O atoms as well as the similar local B coordination. Previous measurements on both the B *K* and N *K* edges of several polymorphs of BN (Hosoi et al., 1982; Terminello et al., 1994) have already identified the π^* and σ^* features in the spectra of h-BN and the σ^* feature in the spectra of c-BN that arise from their differing local coordinations.

Boron oxide (B_2O_3) occurs in two principal polymorphs: glassy and crystalline. The glassy form is most common. The glassy structure is still debated, although the consensus is that the B is predominantly threefold-coordinated to O, comprising a random network of boroxol rings (Mozzi and Warren, 1970; Prabakar et al., 1990). This coordination is confirmed by its B *K* edge, which is similar in shape to the B *K* edges of minerals containing BO_3 units. Crystalline varieties of B oxide are difficult to prepare (Prewitt and Shannon, 1968; Gurr et al., 1970) and have not been studied in this work.

Quantification of the [3]B/[4]B ratio

Borates containing both BO_3 and BO_4 groups are common. The four mixed [3]B- and [4]B-containing minerals studied have the following [3]B/[4]B ratios: tunellite = 1 (3Δ + 3T); preobrazhenskite = 0.64 (4Δ + 7T); and boracite and chambersite = 0.167 (1Δ + 6T). The terms in parentheses refer to the number of triangles, Δ, and tetrahedra, T, in the fundamental borate building block. In Figure 4, the spectra from the mixed-coordination B minerals are arranged in order of decreasing height of the first π^* peak, at 194 eV (characteristic of [3]B), relative to the intensity of the second peak at ca. 199 eV. This ordering from tunellite to boracite directly follows the decrease in the [3]B/[4]B ratio determined from crystallographic data. As the [3]B/[4]B ratio decreases, the B *K* edge more closely resembles that of [4]B, and in boracite and chambersite, the B *K* ELNES is similar in shape to that of rhodizite. The present data suggest that the B *K* ELNES of the mixed-coordination B minerals is just the superposition of the B *K* edges of B from the respective BO_3 and BO_4 units, which would follow if the characteristic final states for excitation at both [3]B and [4]B sites were sufficiently localized as to prevent significant interaction.

Analysis of the B *K* edges in minerals containing both [3]B and [4]B should therefore allow the [3]B/[4]B ratio to be determined. This is in agreement with the findings of Sauer et al. (1993), who quantified the fraction of B atoms in [3]B sites, f_Δ, in two hydroxyborates by assuming that this fraction was proportional to the intensity in the π^* peak, $J(\pi^*)$, relative to the total integrated intensity in a sufficiently large energy window above the edge onset, $J(\Delta E)$. A similar analysis was employed to determine the fraction of sp^2 bonding relative to sp^3 bonding in carbonaceous materials (Katrinak et al., 1992). We used a procedure similar to that used by Sauer et al. (1993), namely

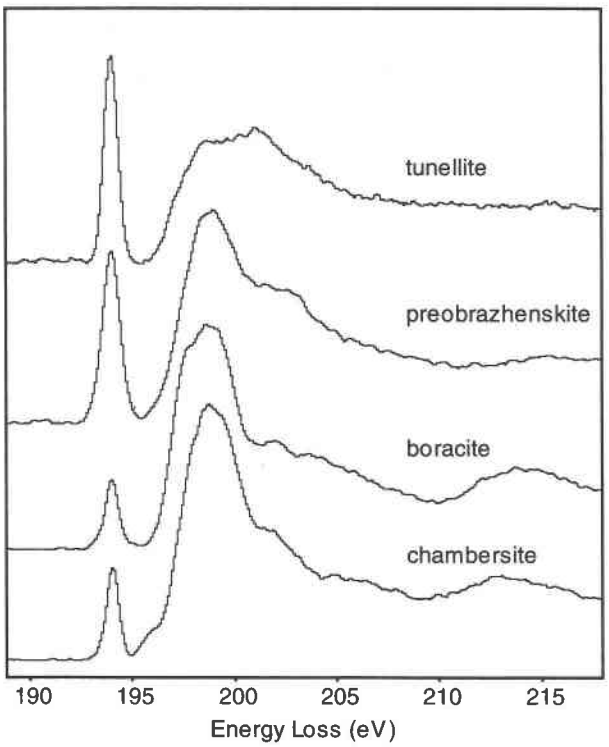

Fig. 4. Experimental PEELS B *K*-edge spectra from minerals containing both [3]B and [4]B. The spectra have been arranged from top to bottom with respect to decrease in the π^*/σ^* height ratio, thus reflecting a decrease in the [3]B/[4]B ratio.

$$f_\Delta = \frac{[J(\pi^*)/J(\Delta E)]}{[J(\pi^*)/J(\Delta E)]_{\text{ref}}}.$$

Here we take $J(\pi^*)$ to be the intensity in a 2.5 eV window over the π^* peak, and $J(\Delta E)$ is the intensity in an energy window of width 14.6 eV commencing 1.4 eV above the π^* peak. The chosen energy window for $J(\pi^*)$ measured the intensity of the whole π^* peak but excluded the intensity in the σ^* region. The energy window ΔE for $J(\Delta E)$ was chosen following two guidelines: first, it must be wide enough so as not to be governed by changes in the ELNES; and second, the window must not extend too far above the edge onset where multiple scattering effects are most dominant. The denominator in the above equation refers to the ratio of spectral intensities in the B *K* edge of a reference material assumed to contain 100% [3]B. We take $[J(\pi^*)/J(\Delta E)]_{\text{ref}}$ to be 0.354, which represents an average value obtained from the [3]B minerals ludwigite (0.353), gaudefroyite (0.256), hambergite (0.401), sussexite (0.395), and glassy B_2O_3 (0.363).

The results of the above procedure for determining f_Δ in the mixed-coordination B minerals are presented in Table 3 together with the theoretical values based on the crystal structures. There is a good match between the theoretical and experimental values for preobrazhenskite, chambersite, and boracite, whereas the fraction of [4]B for tunellite was overestimated. The result from tunellite will be discussed in more detail in the next section.

Table 3. Fraction of [3]B-coordinated sites, f_Δ, derived from the crystal structure (theoretical) and from analysis of the B *K* ELNES using the procedure described in the text

Mineral	f_Δ(theoretical)	f_Δ(experimental)
Tunellite	0.50	0.42
Preobrazhenskite	0.36	0.35
Chambersite	0.14	0.12
Boracite	0.14	0.12

It is difficult to estimate the accuracy of the [3]B/[4]B ratios determined from the B *K* edge using EELS (or XAS). A more systematic study is needed to examine a larger set of materials with a wide range of [3]B/[4]B values. We see that the overall shapes of the B *K* edges are characteristic of B coordination, implying that the ELNES are dominated by the effects of the nearest-neighbor atoms, with minor contributions from atoms surrounding the BO_3^{3-} or BO_4^{5-} anions. This insensitivity of the B *K* edge to the structure outside the immediate coordination sphere is likely to make the determination of the polyanion difficult or impossible, e.g., it is difficult to differentiate between the isolated BO_3^{3-} unit and the triborate polyanion $[B_3O_3(OH)_6]^{3-}$, both of which contain only [3]B. Likewise, the distinction between B coordinated to O anions and B coordinated to OH is likely to be difficult because of the similar scattering powers of both anions.

Use of EELS (or XAS) to determine the coordination-specific site occupancy is likely to find wide application in the study of borate glasses, where the coordination and coordination ratio vary with B content (Prabakar et al., 1990; Müller et al., 1993). Determination of coordination and coordination ratios of B in glasses is typically reserved for ^{11}B MAS NMR, although PEELS conducted in a TEM offers the unequaled advantage of being able to analyze nanometer-sized regions.

Orientation effects

The orientation dependence of core-loss edges was studied in anisotropic materials by EELS and XAS. Orientation dependence arises because of the directionality of the transitions to the unoccupied states into which the bound electron is excited. In XAS, the polarization vector selects the direction probed within the crystal, whereas in EELS, the scattering vector, **q**, selects the direction. In EELS, the direction of **q** is determined by the difference between the wave vectors of the incident and the scattered high-energy electrons. If the incident electrons have an angular divergence that is much less than the characteristic angle of the inelastic scattering process, θ_E, and the angular range over which the scattered electrons are collected is also much less than θ_E, then the direction of **q** is well defined. If the angle of scattering is zero, then **q** is parallel to the incident beam, but if the scattering angle is much greater than θ_E, **q** is approximately perpendicular to the incident beam. This allows the ELNES to be studied as a function of scattering angle and crystal orientation (Leapman et al., 1983). Many polarized studies have

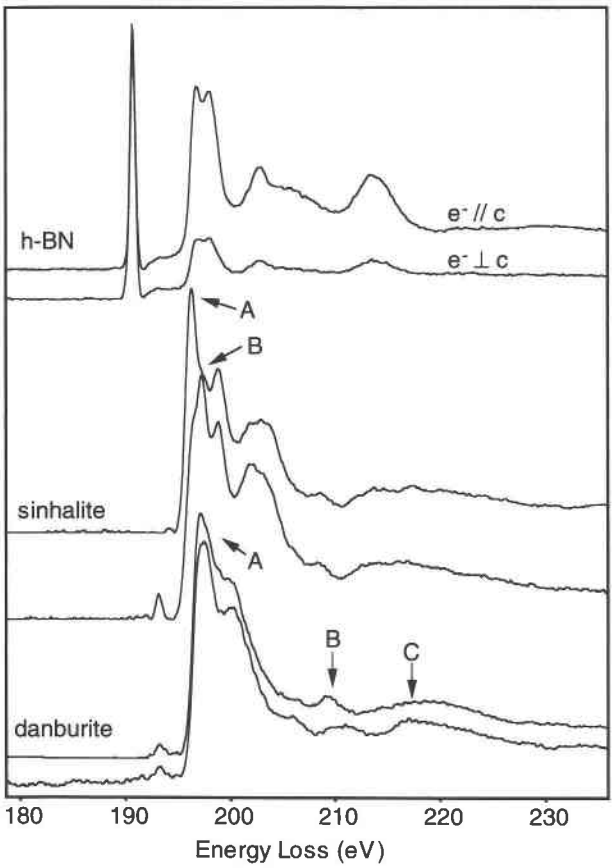

Fig. 5. Spectra from h-BN, sinhalite, and danburite illustrating orientation effects. The B *K* edges for h-BN are for the electron beam parallel ($e^- \parallel$ **c**) and perpendicular ($e^- \perp$ **c**) to the **c** axis. The spectra for h-BN have been normalized at the π^* peak. For sinhalite and danburite, orientation of the electron beam with respect to the axes of the BO_4 tetrahedra is not known. An intermediate spectrum for sinhalite is illustrated in Fig. 2. The small prepeak at ca. 194 eV in sinhalite and danburite is caused by electron-beam damage.

been conducted on graphite because of its anisotropic structure (Leapman et al., 1983; Cheung, 1985; Rosenberg et al., 1986). The basic structure of graphite consists of σ bonding between the C atoms perpendicular to the **c** axis and the π bonds parallel to the **c** axis. When the polarization vector in XAS, or **q** in EELS, is parallel to the **c** axis, states of π character are greatly enhanced over those with σ character, whereas if the vector is perpendicular to the **c** axis, the reverse is true. The EELS experiments reported here differ from the above situation because the sum of the angular divergence of the incident electrons and the angular range over which the scattered electrons are collected is much less than θ_E. The electron beam is focused into a probe with the half angle of convergence of 11 mrad, and the scattered electrons are collected over a cone with the half angle of 12.5 mrad having a mean scattering angle of zero but a range of scattering angles that exceeds θ_E by an order of magnitude. Hence, scattering events over a wide range of **q** vectors are collected, and those with **q** perpendicular to the electron beam are dominant. In this situation, an electron probe incident parallel to the **c** axis ($e^- \parallel$ **c** axis) of graphite results in the detection of more excitations into states of σ character than into states of π character, whereas a probe incident perpendicular to the **c** axis ($e^- \perp$ **c** axis) results in detection of similar numbers of excitations into states of each character. Although orientation effects were not explicitly studied in this work, they were visible in the spectra recorded from several materials and can be used to explain the incorrect $^{[3]}B/^{[4]}B$ ratio determined for tunellite.

Figure 5 illustrates orientation-dependent spectra from h-BN, sinhalite, and danburite. Hexagonal BN has a structure similar to graphite, with σ bonds between the B and N atoms (i.e., perpendicular to the **c** axis) and π orbitals parallel to the **c** axis. In the case of h-BN, Figure 5 shows that the π^* peak is significantly enhanced relative to the σ^* peaks when $e^- \perp$ **c** axis in comparison with the case when $e^- \parallel$ **c** axis. Sinhalite and danburite exhibited a range of ELNES shapes (the main differences are labeled A–C), although the changes were subtle in danburite. The B *K* ELNES of sinhalite can be explained in light of the distorted BO_4 tetrahedra, which have three similar and one long B-O bond length (1.442 Å, 2 × 1.483 Å, and 1.586 Å; Hayward et al., 1994). Thus, the orientation-dependent near-edge structure depends on whether the electron beam is parallel or perpendicular to the long B-O bond. The differences in the B *K* edge of danburite are more difficult to explain. In danburite, B is present in separate B_2O_7 groups with the $B\text{-}O_{br}\text{-}B$ bond (O_{br} = bridging O) roughly parallel to the **c** axis, and the $B\text{-}O_{br}$ distance is shorter than the remaining B-O distances (Phillips et al., 1974). It is probable that the bonds between B and the bridging O have slightly different characteristics than the bonds between B and the nonbridging O atoms. Thus, we would expect differences in the B *K* ELNES depending on whether the incident electron beam is parallel or perpendicular to the **c** axis.

Turning now to the compounds containing the planar BO_3^{3-} group, if the BO_3^{3-} triangles are arranged in several orientations within a crystal, as in glassy B_2O_3, gaudefroyite, and hambergite, then we would not expect to see significant orientation effects. On the other hand, if the planes of the triangles are all aligned, then such orientation effects may be observed. For example, if the incident electron beam is perpendicular to the BO_3^{3-} triangle, then the σ^* region is enhanced in relation to the π^* region (assuming that the sum of the convergence and scattering angles is $\gg \theta_E$, as in the experimental conditions used to record the spectra here). However, determination of the $^{[3]}B/^{[4]}B$ ratio depends on the value of $J(\pi^*)/J(\Delta E)$ from the $^{[3]}B$ component being approximately equal to $[J(\pi^*)/J(\Delta E)]_{ref}$. If the electron beam is perpendicular to the BO_3^{3-} triangles, then $J(\pi^*)/J(\Delta E)$ decreases as a result of the increase of the σ^* region from the $^{[3]}B$ component, with a corresponding decrease in f_Δ and overestimation of $^{[4]}B$.

We are now in a position to explain the anomalously

TABLE 4. Unoccupied orbitals calculated by the SCF-LCAO MO method on a BO_3^{3-} anion (D_{3h} symmetry) using the Gaussian 90 code of Frisch (1990) and STO-3G basis sets

Orbital	Atomic character	Relative energy*	Relative energy**
a_2''	B $2p_z$ + O 2p	211.0	0.0
a_1'	B 2s + O 2s + O 2p	221.8	10.8
e'	B $2p_x$ + B $2p_y$ + O 2s + O 2p	227.7	16.7

Note: The B-O bond length is 1.31 Å.
* Energy relative to the B 1s level at −169.4 eV.
** Energy of the first unoccupied MO.

TABLE 5. Unoccupied orbitals calculated by the SCF-LCAO MO method on a BO_4^{5-} anion (T_d symmetry) using the Gaussian 90 code of Frisch (1990) and STO-3G basis sets

Orbital	Atomic character	Relative energy*	Relative energy**
t_2	B 2p + O 2p	221.2	0.0
a_1	B 2s + O 2p	223.1	1.9

Note: The B-O bond length is 1.46 Å.
* Energy relative to the B 1s level at −153.7 eV.
** Energy of the first unoccupied MO.

low value of f_Δ determined for tunellite from its B *K* edge. In tunellite, the BO_3^{3-} triangles are condensed into an infinite sheet parallel to the (100) plane. Another important feature of tunellite is its perfect {100} cleavage. Drying the finely divided mineral in suspension onto the lacy carbon film resulted in alignment of the thin mineral flakes parallel to the carbon film and thus perpendicular to the electron beam. Therefore the B *K* edges of tunellite were invariably recorded with the electron beam perpendicular to (100), and so $J(\pi^*)/J(\Delta E)$, from the $^{[3]}$B component of tunellite, would be less than $[J(\pi^*)/J(\Delta E)]_{ref}$, giving rise to the anomalously low value of f_Δ and overestimation of the $^{[4]}$B component.

Interpretation of the B *K* ELNES

ELNES may be interpreted and modeled by a variety of techniques (Brydson, 1991; Rez et al., 1991, 1995; Rez, 1992). In terms of single-electron theory, the transitions that result in the observed ELNES simply reflect the unoccupied electronic structure of the solid projected onto the particular atomic site in question. Interpretation of the edges is most easily achieved by comparison with the results of band structure, multiple scattering (MS), or molecular orbital (MO) calculations. These one-electron calculations neglect the interactions between the core hole, created during the excitation process, and the resultant final state. Such interactions may have appreciable effects upon the shape of the ELNES and generally result in a distortion of the electronic structure close to the onset of the conduction band. Core-hole effects are probably most dominant in low atomic number materials, which have few valence electrons with which to shield the hole left by the excitation process (Brydson et al., 1988a; Weijs et al., 1990). For example, the large prepeak to the B *K* edge of β-B_{105} is thought to be caused by the interaction of the core hole with the conduction-band final states, resulting in the formation of a separate unoccupied energy level below the conduction-band onset (P. Rez, personal communication).

The spectra of the minerals presented here are compared with our own SCF-LCAO (self-consistent field linear combination of atomic orbitals) calculations on BO_3^{3-} and BO_4^{5-} anions using the Gaussian 90 code of Frisch (1990) and STO-3G basis sets, the corresponding MO calculations of Vaughan and Tossell (1973), and the results of cluster-based MS calculations using the ICXANES program (Vvedensky et al., 1986). MO theory was used to interpret qualitatively ELNES by comparing the results of the calculations with the features observed within the first few electron volts of the ionization edge onset.

Molecular orbital theory

The symmetry of the O or OH ligands surrounding the B atoms determines the energies and degeneracy of the unoccupied molecular orbitals. In icosahedral (I_h), octahedral (O_h), and tetrahedral (T_d) symmetries the B p orbitals are triply degenerate and belong to a MO of t_2 character. Reduction of the degeneracy occurs in hexagonal (D_{6h}), tetragonal (D_{4h}), and triangular (D_{3h}) symmetries, with the p_z orbital being of a_2'' character and the p_x and p_y orbitals being of e' character. Distortions in the symmetry of the ligands from the ideal T_d or D_{3h} symmetry are expected to cause degenerate levels to lose their degeneracy, and this would be manifested in the ELNES either as a broadening or splitting of features. The differences between the B *K* ELNES of $^{[3]}$B and $^{[4]}$B may be explained by the different unoccupied MOs of the two anions. The relative energies of these unoccupied MOs are given in Tables 4 and 5. In BO_3^{3-}, the lowest unoccupied MO (LUMO) is the a_2'' (π^*) antibonding MO, which is derived from B 2p electrons, followed by the a_1' (σ^*) and the doubly degenerate e' (σ^*) MOs, which are predominantly B 2s and B 2p in character, respectively (Vaughan and Tossell, 1973). Our own MO calculations, as well as those of Vaughan and Tossell (1973), indicate that there is considerable mixing in the a_2'' state between the B and O 2p electrons. Addition of another O atom and rearrangement to form the BO_4^{5-} anion (with B in T_d site symmetry) significantly change the MO structure. The LUMO becomes the triply degenerate t_2 (σ^*) MO derived from B 2p states, closely followed by the a_1 (σ^*) MO, which is predominantly B 2s in character.

The B *K* edges of minerals that contain only BO_3 groups all have two main structures: an initial intense peak (peak A, Fig. 1) followed by a broader peak that varies in intensity and shape. It is now fairly well agreed that the first sharp peak of the B *K* edge of h-BN (Barth et al., 1980) and BF_3- (Ishiguro et al., 1982; Schwarz et al., 1983) and BO_3-containing minerals (Sauer et al., 1993) is the result of transitions to an unoccupied π MO. For $B(OH_3)$

TABLE 6. Unoccupied orbitals calculated by the SCF-LCAO MO method on a BO_4^{5-} anion (C_s symmetry) using the Gaussian 90 code of Frisch (1990) and STO-3G basis sets

Orbital	Atomic character	Relative energy*	Relative energy**
a′	B $2p_x$ + B $2p_y$ + O 2p	217.7	0.0
a′	B 2s + B $2p_x$ + B $2p_y$ + O 2s + O 2p	220.3	2.6
a″	B $2p_z$ + O 2p	220.7	3.0
a′	B 2s + B $2p_x$ + B $2p_y$ + O 2s + O 2p	224.1	6.4

Note: The B-O bond lengths and angles for sinhalite are from Fang and Newnham, 1965.

* Energy relative to the calculated energy of the B 1s level at −154.1 eV.

** Energy of the first unoccupied MO.

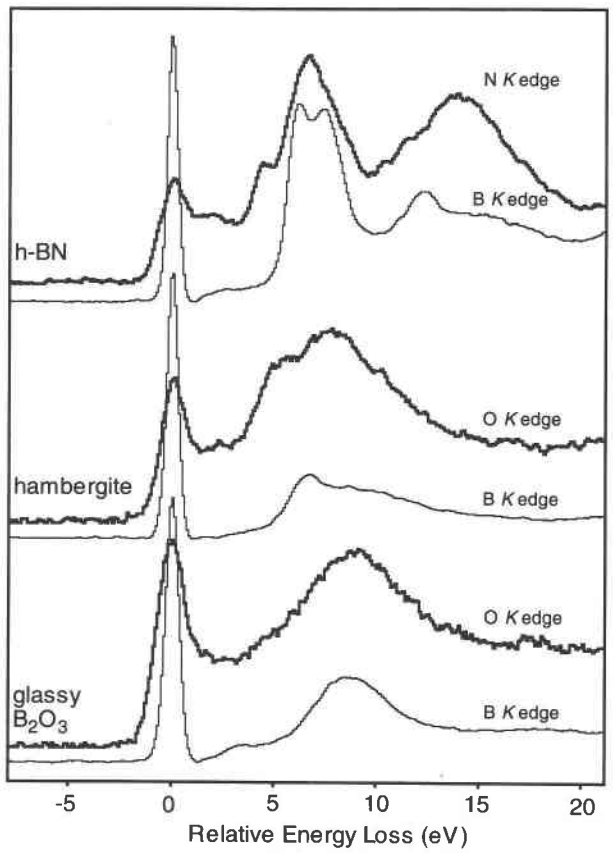

Fig. 6. Comparison of the B *K* edge (thin line) with the corresponding anion *K* edge (thick line) for h-BN, hambergite, and glassy B_2O_3. The π^* peaks from the B *K* edges are aligned with the first peak from the anion *K* edges, and the spectra are presented on a relative energy scale.

and BF_3, this first peak is described as a B $2p\pi$ nonbonding or weakly antibonding orbital of a_2 symmetry (Tossell, 1986). The broad peak C, centered 7–10 eV higher in energy, then corresponds to transitions from a 1s to an e′ (σ^*) MO, which is dominantly B 2p in character. The energy separation between these features in the experimental spectra is in reasonable agreement with the theoretical separation derived from our MO calculations on BO_3^{3-} (Table 4). Several of the spectra show a weak peak, B, between the π^* and σ^* peaks, and this could be interpreted as a dipole-forbidden 1s → a_1' (σ^*) transition. A transition to this B 2s-like state would explain the weakness of this peak. An alternative explanation for the presence of this feature, and some of the other features such as peaks B′ and D from ludwigite, involves the influence of more distant atoms (i.e., next-nearest neighbor and beyond). Such effects are more easily handled using a multiple scattering approach and are discussed later.

The π^* peak present in the [3]B *K* edge corresponds to a transition to a bound state lying below the conduction-band onset at 195.7 ± 0.5 eV (Brydson et al., 1992). The latter figure was derived from XPS measurements of the energy separation between the B 1s peak and the top of the valence band together with the magnitude of the band gap obtained directly from EELS low-loss measurements. This suggests that the position, and presumably intensity, of the π^* feature is strongly affected by interaction with the 1s core hole left by the excitation process.

The high-energy resolution of the HB5 STEM facility allows the true width of the π^* peak from [3]B to be determined, provided that the width of the π^* peak is greater than the width of the zero-loss peak. The width of the π^* peak varies from ca. 0.6 eV in dumortierite, ludwigite, and hambergite, to ca. 0.9 eV in sussexite, to 1.5 eV in gaudefroyite. The lower value of 0.6 eV is limited by the width of the zero-loss peak, which always exhibited a full-width half-maximum (FWHM) of 0.45–0.54 eV during the acquisition of the B *K* edges. Barth et al. (1980) measured a FWHM of 0.4 eV for the π^* peak from h-BN. Our measurement for the width of the π^* peak from h-BN of 0.59 eV is consistent with the width of the zero-loss peak. As mentioned above, distortions of the environment around B in the BO_3 group are expected to cause broadening of the ELNES features. In dumortierite, ludwigite, hambergite, and gaudefroyite, B sits in regular [3]B sites with three similar B-O bond lengths (Zachariasen et al., 1963; Moore and Araki, 1978; Bonazzi and Menchetti, 1989; Garvie et al., in preparation). The larger width of the π^* peak from sussexite is probably caused by the distorted BO_3^{3-} triangle (Hoffmann and Armbruster, 1995) with B-O bond lengths of 1.370–1.408 Å, which deviate significantly from the average value of 1.365 Å found for the BO_3 anion. The cause of the larger π^* peak from gaudefroyite is uncertain because the BO_3 triangle is regular, although a contributing factor may be the two inequivalent B-O bonds. In gaudefroyite, two of the O atoms are twofold coordinated, whereas the third O atom is threefold coordinated.

Although the spectra for [4]B all show considerable differences in their near-edge structure, they are characterized by a sudden increase in the intensity at ca. 196–198 eV. The MO picture for BO_4^{5-} (Vaughan and Tossell, 1973) shows one dipole-accessible MO, t_2 (σ^*) of B 2p character. Thus, the first peak (peak A, Fig. 2) may be assigned to

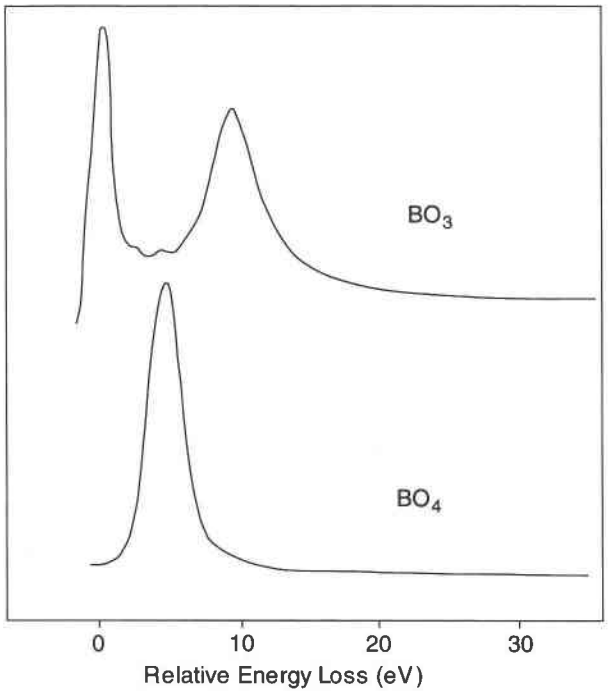

Fig. 7. Theoretical multiple scattering calculations of the B *K* edge for a trigonal BO_3 cluster and a tetrahedral BO_4 cluster. The calculations have been conducted for a one-shell cluster.

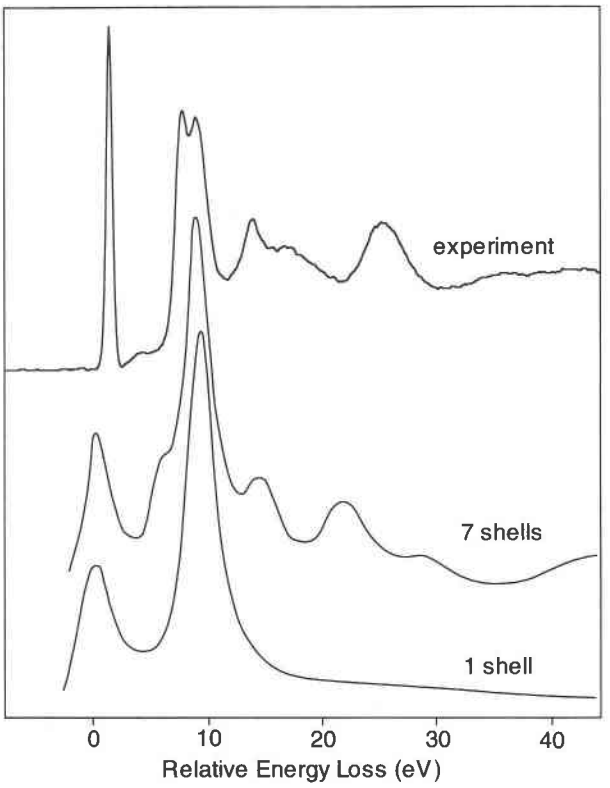

Fig. 8. Comparison of the theoretical multiple scattering calculations for h-BN with an experimental B *K* edge. The multiple scattering calculations for one- and seven-shell clusters are illustrated.

transitions to the triply degenerate t_2 (σ^*) MO. The MO picture for BO_4^{5-} shows another unoccupied MO, the a_1 (σ^*), but because this is of predominantly B 2s character (Vaughan and Tossell, 1973), transitions from the 1s core level to the a_1 (σ^*) MO are dipole forbidden and hence weak. In rhodizite, B is sited in regular tetrahedral sites (Pring et al., 1986) with only small angular and bond variations from an ideal tetrahedron (T_d). Thus, the B *K* ELNES of rhodizite can be described as an archetypal $^{[4]}$B *K* edge. Its edge is dominated by the intense σ^* peak, A, followed by several weaker, broader structures (Fig. 2, Table 2). All these peaks are present in sinhalite, but they are more intense relative to the first σ^* peak. The extra structures in sinhalite relative to the spectrum from rhodizite result from the highly distorted BO_4 tetrahedron (angular variance 56.87°^{2}), with B-site symmetry C_S (Hayward et al., 1994). This distortion causes the triply degenerate t_2 (σ^*) MO to lose its degeneracy and split into two MOs, a″ (p_z) and a doubly degenerate a′ (p_x and p_y). The MO structure of such a distorted BO_4 tetrahedron is tabulated in Table 6. Qualitatively, the observed experimental peak separations agree well with the separation between the calculated MO levels.

Finally, because the states probed by the excited electron are essentially hybridized states consisting of both B 2p and O 2p character, one would expect to see analogous features at the O *K* edge, which essentially probe O 2p-derived unoccupied states. Indeed, the O *K* ELNES of borates and borosilicates containing $^{[3]}$B exhibits a sharp feature at ca. 532 eV corresponding to transitions to the π^* MO (Sauer et al., 1993). In Figure 6 we compare the B and N *K* edges of h-BN and the B and O *K* edges of glassy B_2O_3 and hambergite. Most of the fine structure visible at the anion *K* edge is present at the cation *K* edge, thus attesting to the idea of hybridization between anion and cation electrons of p-like character.

Multiple-scattering theory

Multiple-scattering (MS) theory is based on interference between the outgoing electron wave of the excited electron and the electron wave backscattered from the surrounding atoms. MS calculations are performed in real space using a cluster approach and, in the limit of large cluster size, are formally equivalent to electronic band structures calculated using Korringa-Kohn-Rostocker (KKR) theory. The scattering properties of the various atoms in the cluster are described by phase shifts obtained by integration of the Schrödinger equation, assuming a muffin tin form for the crystalline potential. It is this assumption that often limits the accuracy of the overall MS calculation, especially in open structures, such as minerals, which possess substantial directionality (i.e., covalence) in the bonding.

The cluster approach readily permits the investigation of the influence of different shells of neighboring atoms on the overall ELNES and may be used to identify the

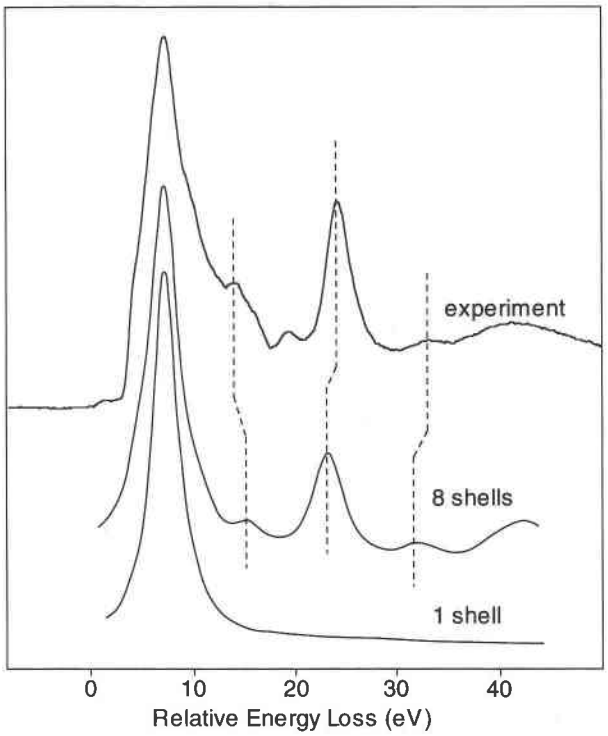

Fig. 9. Comparison of the theoretical MS calculations for c-BN with an experimental B *K* edge. The MS calculations for one- and eight-shell clusters are shown.

existence of coordination fingerprints (i.e., ELNES structures predominantly determined by the arrangement and type of atoms in the nearest-neighbor coordination shell). Furthermore, excited atom potentials can be included so as to simulate the effect of the core hole on near-edge features (Brydson et al., 1988a, 1988b). The energy scale of MS calculations is entirely relative, and the usual procedure is to align the initial features present in both experiment and theory. Further details of the XANES calculation may be found in Vvedensky et al. (1986) and Brydson (1991).

To demonstrate the existence of specific coordination fingerprints for $^{[3]}$B and $^{[4]}$B in borate and borosilicate minerals, we present the results of MS calculations on planar trigonal BO_3 and tetrahedral BO_4 clusters in Figure 7. Core-hole effects were included by use of the $(Z + 1)^*$ approximation for the central B atom in the cluster. O atoms and ions are particularly strong backscatterers, and their spatial arrangement in the nearest-neighbor coordination shell dominates the overall near-edge structure obtained. In the case of $^{[3]}$B, we are able to model the observed π^* and σ^* features common to the experimental spectra of Figure 1, whereas for $^{[4]}$B we obtain only an isolated σ^* feature. It is now our belief that some of the additional structures observed after the initial peak in the experimental spectra shown in Figures 1 and 2 arise from more distant shells of atoms than the nearest-neighbor shell, thus explaining some of the differences observed between $^{[4]}$B-containing minerals.

Similar results may be obtained for the polymorphs of BN. Figures 8 and 9 show the results of MS calculations on h- and c-BN, respectively. Core-hole effects were again included. The clusters employed consisted of seven and eight shells, respectively, and in each case were >0.5 nm in radius in an attempt to reproduce all the observed features. Although all details are not reproduced, the overall agreement is satisfactory. Also in Figures 8 and 9, we show calculations on smaller clusters consisting of one shell of N atoms threefold- and fourfold-coordinated to a central B atom. These calculations essentially confirm the existence of a B *K* ELNES coordination fingerprint. In the case of h-BN, they reproduce the sharp π^* and σ^* features expected on the basis of MO theory, whereas for c-BN we observe only the broader σ^* feature.

Acknowledgments

We would like to thank the following for donating specimens: J. Faithfull (Huntarian Museum, Glasgow, U.K.) for the specimen of axinite (M8304); L. Greenbank (Cumbria, U.K.) for the boracite; G. Cressey (British Museum of Natural History, London) for the hambergite (BM 1911,1); and A. Hodgkinson (Glasgow, U.K.) for the sinhalite gemstone. We would also like to thank the University of London Computer Center for help in the MO calculations, and the Science and Engineering Research Council for the Gatan 666 PEELS and for a postdoctoral research assistantship for L.A.J.G.

References cited

Barth, J., Kunz, C., and Zimkina, T.M. (1980) Photoemission investigation of hexagonal BN: Band structure and atomic effect. Solid State Communications, 36, 453–456.

Bonazzi, P., and Menchetti, S. (1989) Contribution to the crystal chemistry of the minerals of the ludwigite-vonsenite series. Neues Jahrbuch für Mineralogie Monatshefte, 2, 69–83.

Browning, N.D., Chisholm, M.F., and Pennycook, S.J. (1993) Atomic-resolution chemical analysis using a scanning transmission electron microscope. Nature, 366, 143–146.

Bruley, J., Hoche, T., Kleebe, H.-J., and Rühle, M. (1994) Recent attempts to detect magnesium in a heavily doped sapphire bicrystal by spatially resolved electron energy-loss spectroscopy. Journal of the American Ceramic Society, 77, 2273–2276.

Brydson, R. (1991) Interpretation of near-edge structure in the electron energy-loss spectrum. Electron Microscopy Society of America Bulletin, 21, 57–67.

Brydson, R., Bruley, J., and Thomas, J.M. (1988a) Further evidence for core-hole effects in the near-edge structures of light-element *K*-edges. Chemical Physics Letters, 149, 343–347.

Brydson, R., Vvedensky, D.D., Engel, W., Sauer, H., Williams, B.G., Zeitler, E., and Thomas, J.M. (1988b) Chemical information from electron-energy-loss near-edge structure: Core hole effects in the beryllium and boron *K*-edges in rhodizite. Journal of Physical Chemistry, 92, 962–966.

Brydson, R., Williams, B.G., Engel, W., Lindner, Th., Muhler, M., Schlogl, R., Zeitler, E., and Thomas, J.M. (1988c) Electron energy-loss spectroscopy and the crystal chemistry of rhodizite: Part 2. Near-edge structure. Journal of the Chemical Society, Faraday Transactions, 84, 631–646.

Brydson, R., Sauer, H., and Engel, W. (1992) Electron energy loss near-edge structure as an analytical tool: The study of minerals. In M.M. Disko, C.C. Ahn, and B. Fultz, Eds., Transmission electron energy loss spectrometry in materials science, p. 131–154. The Minerals, Metals and Materials Society, Warrendale, Illinois.

Burns, P.C., and Hawthorne, F.C. (1994) Structure and hydrogen bonding in preobrazhenskite, a complex heteropolyhedral borate. Canadian Mineralogist, 32, 387–396.

Cheung, T.T.P. (1985) Orientation dependence of the carbon *K* edge in

graphite measured by reflection electron-energy-loss spectroscopy. Physical Review B, 31, 4792–4797.

Christ, C.L., and Clark, J.R. (1977) A crystal-chemical classification of borate structures with emphasis on hydrated borates. Physics and Chemistry of Minerals, 2, 59–87.

Clark, J.R. (1964) The crystal structure of tunellite, $SrB_6O_9(OH)_2 \cdot 3H_2O$. American Mineralogist, 49, 1549–1568.

Dowty, E., and Clark, J.R. (1973) Crystal-structure refinements for orthorhombic boracite, $Mg_3ClB_7O_{13}$, and a trigonal, iron-rich analogue. Zeitschrift für Kristallographie, 138, 64–99.

Egerton, R.F. (1986) Electron energy-loss spectroscopy in the electron microscope, 410 p. Plenum, New York.

Esposto, F.J., Aebi, P., Tyliszczak, T., Hitchcock, A.P., Kasrai, M., Bozek, J.D., Jackman, T.E., and Rolfe, S.R. (1991) Boron *K*-shell spectroscopy of boron-doped silicon. Journal of Vacuum Science and Technology, A9, 1663–1669.

Fang, J.H., and Newnham, R.E. (1965) The crystal structure of sinhalite. Mineralogical Magazine, 35, 196–199.

Farmer, J.B. (1982) Metal borates. Advances in Inorganic Chemistry and Radiochemistry, 25, 187–237.

Foit, F.F., Jr., Phillips, M.W., and Gibbs, G.V. (1973) A refinement of the crystal structure of datolite, $CaBSiO_4(OH)$. American Mineralogist, 58, 909–914.

Frisch, M.J. (1990) GAUSSIAN 90 revision I. Gaussian, Pittsburgh, Pennsylvania.

Fuggle, J.C., and Inglesfield, J.E., Eds. (1992) Unoccupied electronic states: Fundamentals for XANES, EELS, IPS and BIS, 359 p. Springer-Verlag, New York.

Garvie, L.A.J. (1995) Parallel electron energy-loss spectroscopy of boron in minerals. In Mineralogical Society of America Reviews in Mineralogy, 33, in press.

Garvie, L.A.J., Craven, A.J., and Brydson, R. (1994) Use of electron-energy loss near-edge fine structure in the study of minerals. American Mineralogist, 79, 411–425.

Garvie, L.A.J., Buseck, P.R., and Craven, A.J. (1995) Electron-loss near-edge structure (ELNES) as a valence and site-specific probe. Canadian Mineralogist, in press.

Gurr, G.E., Montgomery, P.W., Knutson, C.D., and Gorres, B.T. (1970) The crystal structure of trigonal diboron trioxide. Acta Crystallographica, B26, 906–915.

Guy, C.N., and Uraz, A.A. (1976) The chromium-boron system. Journal of the Less-Common Metals, 48, 199–203.

Hallmeier, K.-H., Szargan, R., Meisel, A., Hartmann, E., and Gluskin, E.S. (1981) Investigation of core-excited quantum yield spectra of high-symmetric boron compounds. Spectrochimica Acta, A37, 1049–1053.

Hansen, P.L., McComb, D.W., and Brydson, R. (1992) ELNES fingerprints of Al coordination in nesosilicates. Micron and Microscopia Acta, 23, 169–170.

Hayward, C.L., Angel, R.J., and Ross, N.L. (1994) The structural redetermination and crystal chemistry of sinhalite, $MgAlBO_4$. European Journal of Mineralogy, 6, 313–321.

Heller, G. (1986) A survey of structural types of borates and polyborates. Topics in Current Chemistry, 131, 39–98.

Hoard, J.L., Sullenger, D.B., Kennard, C.H.L., and Hughes, R.E. (1970) The structure analysis of β-rhombohedral boron. Journal of Solid State Chemistry, 1, 268–277.

Hofer, F., and Golob, P. (1987) New examples for near-edge fine structures in electron energy loss spectroscopy. Ultramicroscopy, 21, 379–384.

Hoffmann, C., and Armbruster, T. (1995) Crystal structure of a (001) twinned sussexite $Mn_2B_2O_4(OH)_2$ from the Kalahari Manganese Field South Africa. Schweizerische Mineralogische und Petrographische Mitteilungen, 75, 123–133.

Honea, R.M., and Beck, F.R. (1962) Chambersite, a new mineral. American Mineralogist, 47, 665–671.

Hosoi, J., Oikawa, T., and Inoue, M. (1982) Study of boron nitride by electron energy loss spectroscopy. Journal of Electron Spectroscopy and Related Phenomena, 27, 243–254.

Ildefonse, P., Calas, G., Kirkpatrick, R.J., Montez, B., Flank, A.M., and Lagarde, P. (1992) Local environment of aluminium in amorphous alumino-silicates by XANES and MAS NMR. In Y.K. Kharaka and A.S. Maest, Eds., Proceedings of the 7th International Symposium on Water-Rock Interaction, p. 153–158. Balkema, Rotterdam, the Netherlands.

Ildefonse, P., Kirkpatrick, R.J., Montez, B., Calas, G., Flank, A.M., and Lagarde, P. (1994) ^{27}Al MAS NMR and aluminium X-ray absorption near edge structure study of imogolite and allophanes. Clay and Clay Minerals, 42, 276–287.

Ishiguro, E., Iwata, S., Suzuki, Y., Mikuni, A., and Sasaki, T. (1982) The boron *K* photoabsorption spectra of BF_3, BCl_3 and BBr_3. Journal of Physics B: Atomic and Molecular Physics, 15, 1841–1854.

Katrinak, K.A., Rez, P., and Buseck, P.R. (1992) Structural variations in individual carbonaceous particles from an urban aerosol. Environmental Science and Technology, 26, 1967–1976.

Leapman, R.D., Fejes, P.L., and Silcox, J. (1983) Orientation dependence of core edges from anisotropic materials determined by inelastic scattering of fast electrons. Physical Review B, 28, 2361–2373.

Li, D., Bancroft, G.M., Kasrai, M., Fleet, M.E., Feng, X.H., Tan, K.H., and Yang, B.X. (1993) High-resolution Si *K*- and $L_{2,3}$-edge XANES of α-quartz and stishovite. Solid State Communications, 87, 613–617.

Luck, S., and Urch, D.S. (1990) Boron $K\alpha$ XRE and the electronic structure of boron compounds: Coordination and resonance emission. Physica Scripta, 41, 970–972.

Marchetti, P.S., Kwon, D., Schmidt, W.R., Interrante, L.V., and Maciel, G.E. (1991) High-field ^{11}B magic-angle spinning NMR characterization of boron nitrides. Chemistry of Materials, 3, 482–486.

McComb, D.W., Hansen, P.L., and Brydson, R. (1991) A study of silicon ELNES in nesosilicates. Microscopy, Microanalysis, Microstructures, 2, 561–568.

McComb, D.W., Brydson, R., Hansen, P.L., and Payne, R.S. (1992) Qualitative interpretation of electron energy-loss near-edge structure in natural zircon. Journal of Physics: Condensed Matter, 4, 8363–8374.

Meera, B.N., Sood, A.K., Chandrabhas, N., and Ramakrishna, J. (1990) Raman study of lead borate glasses. Journal of Non-Crystalline Solids, 126, 224–230.

Moore, P.B., and Araki, T. (1978) Dumortierite, $Si_3B[Al_{6.75\ 0.25}O_{17.25}(OH)_{0.75}]$ a detailed structure analysis. Neues Jahrbuch für Mineralogie Abhandlungen, 132, 231–241.

Moustafa, Y.M., Doweidar, H., and El-Dawrawi, G. (1994) Utilization of infrared spectroscopy to determine the fraction of the four coordinated borons in borate glasses. Physics and Chemistry of Glasses, 35, 104–106.

Mozzi, R.L., and Warren, B.E. (1970) The structure of vitreous boron oxide. Journal of Applied Crystallography, 3, 251–257.

Müller, D., Grimmer, A.-R., Timper, U., Heller, G., and Shakibaie-Moghadam, M. (1993) ^{11}B MAS NMR studies on the structure of borate anions. Zeitschrift für anorganische und allgemeine Chemie, 619, 1262–1268.

Pease, R.S. (1950) Crystal structure of boron nitride. Nature, 165, 722–723.

Phillips, M.W., Gibbs, G.V., and Ribbe, P.H. (1974) The crystal structure of danburite: A comparison with anorthite, albite, and reedmergnerite. American Mineralogist, 59, 79–85.

Prabakar, S., Rao, K.J., and Rao, C.N.R. (1990) ^{11}B NMR spectra and structure of boric oxide and alkali borate glasses. Proceedings of the Royal Society of London, 429A, 1–15.

Prewitt, C.T., and Shannon, R.D. (1968) Crystal structure of a high-pressure form of B_2O_3. Acta Crystallographica, B24, 869–874.

Pring, A., Din, V.K., Jefferson, D.A., and Thomas, J.M. (1986) The crystal chemistry of rhodizite: A re-examination. Mineralogical Magazine, 50, 163–172.

Rez, P. (1992) Energy loss fine structure. In M.M. Disko, C.C. Ahn, and B. Fultz, Eds., Transmission electron energy loss spectrometry in materials science, p. 107–129. The Minerals, Metals and Materials Society, Warrendale, Illinois.

Rez, P., Weng, X., and Ma, H. (1991) The interpretation of near edge structure. Microscopy, Microanalysis, Microstructures, 2, 143–151.

Rez, P., Bruley, J., Brohan, P., Payne, M., and Garvie, L.A.J. (1995) Calculation of near edge structure. Ultramicroscopy, in press.

Rosenberg, R.A., Love, P.J., and Rehn, V. (1986) Polarization-dependent C(*K*) near-edge-absorption fine structure of graphite. Physical Review B, 33, 4034–4037.

Sauer, H., Brydson, R., Rowley, P.N., Engel, W., and Thomas, J.M. (1993) Determination of coordinations and coordination-specific site occu-

pancies by electron energy-loss spectroscopy: An investigation of boron-oxygen compounds. Ultramicroscopy, 49, 198–209.

Schwarz, W.H.E., Mensching, L., Hallmeier, K.H., and Szargan, R. (1983) *K*-shell excitations of BF_3, CF_4 and MBF_4 compounds. Chemical Physics, 82, 57–65.

Sekiyama, H., Kitajima, Y., Kosugi, N., Kuroda, H., and Ohta, T. (1984) Photon Factory Activity Report 1983/84, VI-119. Tsukuba, Japan.

Sen, S., Stebbins, J.F., Hemming, N.G., and Ghosh, B. (1994) Coordination environments of B impurities in calcite and aragonite polymorphs: A ^{11}B MAS NMR study. American Mineralogist, 79, 819–825.

Sills, J.A., Martin, S.W., and Torgeson, D.R. (1994) ^{11}B NMR studies of the short range order in wide composition range $xNa_2S+(1-x)B_2S_3$ glasses. Journal of Non-Crystalline Solids, 168, 86–96.

Solozhenko, V.L., Chernyshev, V.V., Fetisov, G.V., Rybakov, V.B., and Petrusha, I.A. (1990) Structure analysis of the cubic boron nitride crystals. Journal of Physics and Chemistry of Solids, 51, 1011–1012.

Takeuchi, Y., Ozawa, T., Ito, I., Araki, T., Zoltai, T., and Finney, J.J. (1974) The $B_2Si_8O_{30}$ groups of tetrahedra in axinite and comments on the deformation of Si tetrahedra in silicates. Zeitschrift für Kristallographie, 140, 289–312.

Terminello, L.J., Chaiken, A., Lapiano-Smith, D.A., Doll, G.L., and Sato, T. (1994) Morphology and bonding measured from boron-nitride powders and films using near-edge X-ray absorption fine structure. Journal of Vacuum Science Technology, A12, 2462–2466.

Tossell, J.A. (1986) Studies of unoccupied molecular orbitals of the B-O bond by molecular orbital calculations, X-ray absorption near edge, electron transmission, and NMR spectroscopy. American Mineralogist, 71, 1170–1177.

Turner, G.L., Smith, K.A., Kirkpatrick, R.J., and Oldfield, E. (1986) Boron-11 nuclear magnetic resonance spectroscopic study of borates and borosilicate minerals and borosilicate glass. Journal of Magnetic Resonance, 67, 544–550.

Vaughan, D.J., and Tossell, J.A. (1973) Molecular orbital calculations on beryllium and boron oxyanions: Interpretations of X-ray emission, ESCA, and NQR spectra and of the geochemistry of beryllium and boron. American Mineralogist, 58, 765–770.

Vvedensky, D.D., Saldin, D.K., and Pendry, J.B. (1986) An update of DLXANES, the calculation of X-ray absorption near-edge structure. Computer Physics Communications, 40, 421–440.

Weijs, P.J.W., Czyzyk, M.T., van Acker, J.F., Speier, W., Goedkoop, J.B., van Leuken, H., Hendrix, H.J.M., de Groot, R.A., van der Laan, G., Buschow, K.H.J., Wiech, G., and Fuggle, J.C. (1990) Core-hole effects in the X-ray-absorption spectra of transition-metal silicides. Physical Review B, 41, 11899–11910.

Zachariasen, W.H., Plettinger, H.A., and Marezio, M. (1963) The structure and birefringence of hambergite, $Be_2BO_3 \cdot OH$. Acta Crystallographica, 16, 1144–1146.

Manuscript received December 12, 1994
Manuscript accepted June 27, 1995